Nanoscale

PAPER

View Article Online
View Journal | View Issue



Cite this: *Nanoscale*, 2024, **16**, 6531

# Mono-, bi- and tri-metallic Fe-based platinum group metal-free electrocatalysts derived from phthalocyanine for oxygen reduction reaction in alkaline media†

Seyed Ariana Mirshokraee,[a] Mohsin Muhyuddin,[a] Jacopo Orsilli,[a] Enrico Berretti,[b] Alessandro Lavacchi,[b] Carmelo Lo Vecchio,[c] Vincenzo Baglio,[c] Rosanna Viscardi,[d] Andrea Zaffora,[e] Francesco Di Franco,[e] Monica Santamaria,[e] Luca Olivi,[f] Simone Pollastri[f,g] and Carlo Santoro *[a]

In this manuscript, a comprehensive study is presented on Fe-based electrocatalysts with mono, bi, and tri-metallic compositions, emphasizing the influence of processing-structure correlations on the electrocatalytic activity for the oxygen reduction reaction (ORR) in the alkaline medium. These electrocatalysts were synthesized through the mixing of transition metal phthalocyanines (TM-Pc) with conductive carbon support, followed by controlled thermal treatment at specific temperatures (600 °C and 900 °C). An extensive analysis was conducted, employing various techniques, including X-ray Absorption Spectroscopy (XAS), Transmission Electron Microscopy (TEM), and X-ray Diffraction (XRD), providing valuable insights into the structural characteristics of the synthesized nanoparticles. Importantly, an increase in the Fe–Pc weight percentage from 10% to 30% enhanced the ORR activity, although not proportionally. Furthermore, a comparative analysis between mono, bi, and tri-metallic samples subjected to different functionalization temperatures highlighted the superior electrocatalytic activity of electrocatalysts functionalized at 600 °C, particularly Fe 600 and Fe–Ni–Cu 600. These electrocatalysts featured $E_{on}$ values of 0.96 V *vs.* RHE and $E_{1/2}$ values of 0.9 V *vs.* RHE, with the added benefit of reduced anionic peroxide production. The potential of these Fe-based electrocatalysts to enhance ORR efficiency is underscored by this research, contributing to the development of more effective and sustainable electrocatalysts for energy conversion technologies.

Received 7th February 2024,
Accepted 2nd March 2024

DOI: 10.1039/d4nr00575a

rsc.li/nanoscale



## 1. Introduction

To mitigate anthropogenic global warming and climate change a complete switch to green and renewable energy sources is inevitably important while avoiding the prime reliance on annihilating fossil fuels. In this context, the objectives of the 'Hydrogen Economy' become pertinent, presenting green hydrogen as the safest energy vector.[1–3] A paramount technology in the arena of the 'Hydrogen Economy' is Fuel Cells (FCs) having an unparalleled potential to continuously translate the chemical energy of a fuel (hydrogen) into electrical energy without contributing to the global carbon footprint.[4,5] However, the deployment of FCs on commercial scales is still restricted, mainly due to the employment of scarce and overvalued platinum group metals (PGMs) to catalyze the complex and sluggish oxygen reduction reaction (ORR) at the cathode.[6,7] As a result of scientific developments over the past few decades, nanostructured first-row transition metals (TMs) based electrocatalysts have emerged as reliable candidates to replace PGMs for ORR, particularly for the anion exchange membrane FCs (AEMFCs) where alkaline conditions resolve the corrosion and stability issues that are predominately faced in acidic media.[7–9] Structurally, such electrocatalysts are based

[a]*Department of Materials Science, University of Milano-Bicocca, U5, Via Roberto Cozzi, 55, 20125 Milan, MI, Italy. E-mail: carlo.santoro@unimib.it*
[b]*Istituto di Chimica Dei Composti OrganoMetallici (ICCOM), Consiglio Nazionale Delle Ricerche (CNR), Via Madonna Del Piano 10, 50019 Sesto Fiorentino, Firenze, Italy*
[c]*Istituto di Tecnologie Avanzate per l'Energia "Nicola Giordano" (ITAE), Consiglio Nazionale delle Ricerche (CNR), Via Salita S. Lucia sopra Contesse 5, Messina, 98126, Italy*
[d]*Casaccia Research Center, ENEA, Santa Maria di Galeria, 00123 Rome, Italy*
[e]*Department of Engineering, University of Palermo, Viale delle Scienze, 90128 Palermo, Italy*
[f]*Elettra-Sincrotrone Trieste, Area Science Park, Basovizza, Trieste, Italy*
[g]*Department of Physics, Computer Science and Mathematics, University of Modena and Reggio Emilia, Via Campi 103, 41125 Modena, Italy*
† Electronic supplementary information (ESI) available. See DOI: https://doi.org/10.1039/d4nr00575a

on atomic level embedment of TM with nitrogen coordination in the carbon matrix and are widely known as M–N–Cs.[10–13] M–N–Cs have the potential to substitute PGM electrocatalysts in FC applications.[10,13–18] Such M–N–C electrocatalysts have shown promising results in terms of their electrocatalytic activity, stability, and durability, especially in alkaline environment.[19,20] Moreover, the use of M–N–C electrocatalysts can reduce the cost and environmental impact of electrocatalysts while improving the performance and scalability of energy conversion technologies.[21,22] M–N–Cs can reduce oxygen following a direct 4 electron transfer mechanism or a 2 × 2 $e^-$ transfer, however, the direct tetra-electronic pathway is always preferred. Among different TM, the usage of Fe-based (Fe–$N_x$–C) electrocatalysts has been found to deliver high electrocatalytic performance for the ORR owing to suitable electronic structure and interaction with oxygen when the iron is present in coordination with nitrogen ($FeN_x$).[23] Consequently, significant research has been carried out on Fe–$N_x$–C and their electrocatalytic activity in ORR.[24–28] However, the performance attributes still fall short when compared to state-of-the-art PGM-based electrocatalysts.

Fe–$N_x$–Cs possess a diverse nature of Fe-containing and Fe-free active sites, collaboratively contributing to ORR.[16,29–31] Fe–$N_x$ ($x$ = 2, 3, 4) are believed to be the primary Fe-containing active sites for the ORR[32–34] and can launch direct tetra-electronic ORR, while metal-free moieties mostly participate in bi-electronic reduction pathway or 2 × 2 $e^-$ ORR.[35,36] While the morphology of the carbon backbone is crucial for reagent access and product removal. To introduce $FeN_x$-based and Fe-free (nitrogen-based) active moieties, different organic precursors and salts can be used whereas the iron phthalocyanine (FePc) has acquired significant attention not only due to a concurrent source of Fe and N but also already has a suitable Fe–N configuration.[37] De Oliveira *et al.* reported the non-pyrolytic synthesis of two high-performance ORR electrocatalysts, both utilizing FePc on different carbon-based supports—carbon nanotubes (CNT) and black pearls (BP).[38] They observed enhanced ORR performance by Fe-BP(N) owing to higher defect density, while the Fe-CNT(N) exhibited a slightly higher half-wave potential in alkaline electrolytes due to the increased conductivity of CNTs. Similarly, Zhang *et al.* employed a straightforward method to prepare a series of TMPc/graphitized carbon black (GCB) electrocatalysts for ORR through π–π interaction self-assembly in isopropanol/tetrahydrofuran mixed solution.[39] The DFT calculations emphasized the influence of the central TM atom in the phthalocyanine macrocycle (TMPcs) on ORR performance. Here it is important to underline that TMPcs are electrocatalytically unstable and their activities can be reduced drastically due to involved degradation mechanisms *i.e.* metal removal and/or oxidation by the peroxide intermediates.[40,41] Nevertheless, fixing the TMPcs on carbon by way of temperature-controlled pyrolysis can ensure operational durability.[40,42] However, the pyrolysis parameters, specifically the temperature can modify the active-site structure and hence influence the electrocatalytic performance. To resolve such discrepancies, our group has detailed analyzed the development and transformation of active-site structure in the FePc functionalized carbon-based electrocatalyst during pyrolysis using a combination of *in situ* and *ex situ* techniques.[43] It was categorically witnessed that pyrolysis parameters have a marked influence on the structural evolution and corresponding electrocatalytic activities of the derived electrocatalysts.

Lately, it has been shown that the introduction of the second TM in TM-N-Cs can be beneficial. Meanwhile, other strategies such as using bi and tri-metallic components for improving the activity were considered.[44–49] For instance Xue *et al.* developed FeCr-N-C to improve the performance of ORR in acidic media by using a bi-metallic component.[50] With the same strategy, Hu *et al.* reported the bimetallic $Fe_2Mo$ nanoparticles on N-doped carbon ($Fe_2Mo$/NC) as an efficient and ultra-stable ORR electrocatalyst in alkaline media.[51] Kumar *et al.* studied bimetallic (Fe, Ni) N-doped carbon catalysts using various carbon supports like multi-walled carbon nanotubes (MWCNT), graphene, carbide-derived carbon, Vulcan carbon, and mesoporous carbon (MC) to explore their electrocatalytic activity in ORR for AEMFCs. Among these electrocatalysts, the FeNiN MC and FeNiN MWCNT demonstrated superior performance with excellent half-wave potential for oxygen reduction.[52] Also, Luo *et al.* investigated the accessible active sites of mono- and bimetallic Fe–NC and FeNi–NC catalysts for ORR.[53] This research revealed that while the nature of Fe sites remains similar in both mono- and bimetallic electrocatalysts, the presence of Ni reduces active site density. For improving mass activity in alkaline media, Lüsi *et al.* developed bimetallic PdM/C electrocatalysts (with M being Bi, Pb, or Sn) supported on Vulcan carbon.[54] Comparisons with pure Pd/C electrocatalysts were made, revealing enhanced mass activities in alkaline solution for BiPd and PbPd catalysts

**Carlo Santoro**

*Carlo Santoro got his Ph.D. at the University of Connecticut in 2009, working on microbial fuel cells. He moved to the University of New Mexico in 2013 working on platinum-free electrocatalysts for oxygen reduction reaction and supercapacitive bio-electrochemical systems. Following a spell as Lecturer at the University of Manchester (2020), he joined the University of Milano-Bicocca in 2021 as Assistant Professor and he got promoted to Associate Professor in 2024. He established the Electrocatalysis and Bioelectrocatalysis Lab (EBLab) counting now 8 PhD student, 2 Post Doc and a research portfolio of more than 1 M euro. His work focuses on development of electrocatalysts based on PGM-free electrocatalysts for electrochemical systems. He has published over 127 manuscripts ($H_{index}$ = 46) and holds 2 patents.*

(2× and 1.6×, respectively) while SnPd exhibited lower mass activity. With an innovating approach, a bioinspired electrocatalyst with adjacent Cu and Fe sites has been developed using a directed synthetic pathway, forming a covalent 3D framework in aerogel form by Persky *et al.*[28] This aerogel-based electrocatalyst displays high performance in both half-cell and AEM fuel cell setups, attributed to its unique structure and metal site proximity. In another work, bi-metallic ORR electrocatalysts, derived from pyrolyzed Fe–M (where M = Co, Cu, Ni, and Mn) compounds along with 4-aminoantipyrine, were synthesized using a sacrificial support method by Serov and his colleagues.[55] The impact of iron's interaction with the second metal on ORR catalytic activity was explored by varying the Fe–M ratio, revealing that the addition of a second transition metal to iron substantially enhances the electrocatalytic activity. While using phthalocyanines as a starting material, an efficient bifunctional oxygen electrocatalyst, conjugated polymerized iron-cobalt phthalocyanine (PPcFeCo)/3D-G, was developed by Wang *et al.* through π–π interaction between PPcFeCo and three-dimensional graphene (3D-G).[56] The bimetallic synergistic effect, confirmed by DFT calculation, and π–π interactions enhance the catalytic activity and durability, resulting in excellent electrochemical performance with a high electron transfer number. In another related work by Li and Sui, the integration of transition metal nanoparticles into a porous nitrogen-enriched carbon framework derived from metallophthalocyanine-based conjugated microporous polymers, followed by template-free pyrolysis, proves to be an efficient method for constructing high-performance ORR/OER bifunctional electrocatalysts.[57] Specifically, the heterometallic-doped electrocatalyst conjugated microporous polymers (CMP)-CoFe/C exhibits superior onset potential and current density for both ORR/OER processes compared to its monometallic counterpart, demonstrating great potential as a cost-effective and stable electrocatalyst in fuel cells. Also Wang *et al.* presented the successful synthesis of homodimetallic Pc (FePc–PcFe and CoPc–PcCo) and a heterodimetallic Pc (FePc–PcCo) as ORR catalysts in acidic media.[58] The study reveals that FePc–PcFe exhibits better ORR activity than FePc, attributed to a smaller HOMO–lowest unoccupied molecular orbitals gap, while FePc–PcCo demonstrates comparable activity with FePc–PcFe and superior performance compared to CoPc–PcCo, as supported by spectroscopic and computational analyses. With a similar token of enhancing ORR performance, Kumar *et al.* bimetallic FePc and NiPc-modified nanocarbon-based electrocatalysts delivering high halfwave potential ($E_{1/2}$) of 0.88 V.[52] In a separate study, Kumar and coworkers have also analyzed the mixed TMPcs (FeNi; FeMn; FeCo) -modified MWCNTs synthesized *via* pyrolysis method and FeMnN-MWCNT delivered outstanding onset potential ($E_{on}$) of 0.93 V *vs.* RHE in alkaline media.[59] However, Muhyuddin *et al.* experienced compareable performance of monometallic FePc functionalized activated char and bimetallic FePc and MnPc functionalized activated char with $E_{on}$ equals to 0.94 V in 0.1 M KOH.[60]

In parallel to bimetallic electrocatalysts, the elucidation of the introduction of third TM could also be interesting and hence tri-metallic PGM-free electrocatalysts for ORR were synthesized by Serov *et al.*, incorporating Co, Cu, Ni, and Mn alongside iron.[61] The study systematically examined the influence of these TM on the electrocatalyst's ORR activity and demonstrated a co-catalytic effect between iron and Co, Cu, and Mn, significantly increasing electrocatalytic efficiency. The continuity in morphology among the synthesized materials suggests that varying the TM component does not impact nanostructural features, resulting in promising tri-metallic iron-based electrocatalysts that show potential to replace platinum. With a similar strategy, Liu *et al.* prepared trimetallic FeCoNi-N/CNFs by impregnating electrospun polyacrylonitrile (PAN) nanofibers with solutions containing $Fe(NO_3)_3$, $Co(NO_3)_2$, and $Ni(NO_3)_2$, followed by heat treatment in $NH_3$.[62] The FeCoNi-N/CNF electrocatalysts exhibited excellent electrochemical performance for ORR in acidic media, with the Fe/Co/Ni ratio of 4 : 2 : 1 demonstrating outstanding activity and stability, attributed to surface pores, high N content, pyridinic-N, quaternary-N, and metal nitrides, especially the presence of $Fe_2N$. Also, Muuli *et al.* reported the preparation and characterization of Fe, Co, and Ni phthalocyanine tri-doped electrospun carbon nanofiber-based electrocatalyst material (FeCoNi-CNF) in alkaline media, demonstrating superior activity towards ORR compared to materials prepared with only two transition metal phthalocyanine combinations (Ni/Fe and Ni/Co).[63]

In recent scientific endeavors, PGM-free and TMPc-based electrocatalysts, such as mono, bi, and trimetallic variants of TM-N-Cs, have developed as a focal point in the domain of electrocatalysts for ORR, initiating critical research curiosities. One such query involves improving the features of active-site structures to realize the peak electrocatalytic performance by regulating the pyrolysis conditions and, importantly, temperature. Additionally, clarifying the distinction in the electrocatalytic response of mono and bimetallic TMPc electrocatalysts, while contrasting them with trimetallic counterparts, is indispensable. Another important challenge pertains to the influence of precursor ratios in populating active sites without sacrificing the single-atom configuration and structural integrity of TM-N-Cs. This certifies the best ORR activity, mainly in monometallic electrocatalysts, and examines whether their activities can compete with that of bi or trimetallic variants. Filling such hotspots can be crucial for the development of a reliable PGM-free ORR electrocatalyst for AEMFCs.

To decipher the aforementioned uncertainties herein, a systematic study on the mono, bi and tri-metallic electrocatalyst has been presented. The preparation of Fe-based electrocatalysts was achieved by mixing various transition metal phthalocyanines (TM-Pc) with commercially available conductive Ketjen-Black carbon (KJB) using a ball miller, followed by functionalizing the obtained powders at two distinct temperatures: 600 °C and 900 °C, within an inert atmosphere (through a 1-hour ultra-high-purity argon flow). Initially, electrocatalysts consisting of KJB and FePc were mixed with different weight percentages of NiPc (30%, 20%, and 10 wt%), and their electrocatalytic activity was quantified and compared to evalu-

ate the influence of FePc content on the ORR activity. The subsequent phase of this investigation encompassed exploring the impacts of various components (mono, bi, and trimetallic) while utilizing an aggregate of 30 wt% of TMs-Pc compound to create the Fe-based electrocatalyst samples. Mono-metallic Fe-based electrocatalysts (30 wt% FePc), bi-metallic Fe–Ni electrocatalysts (15 wt% FePc and NiPc respectively), and tri-metallic Ni–Fe–Cu electrocatalysts (10 wt% of NiPc, FePc, and CuPc respectively) were synthesized, and their electrocatalytic activity was measured and compared within an alkaline environment. The influence of synthesis conditions, such as functionalization temperatures, on the comprehensive electrocatalytic activity under alkaline conditions were meticulously scrutinized for each group of samples. The findings derived from this research significantly contribute to the advancement of effective electrocatalysts for ORR, with the aim to replace precious metal-based electrocatalysts.

## 2. Results and discussion

### 2.1. Morphological studies through TEM imaging

The elucidation of the synthesized electrocatalysts begins with a comprehensive assessment of their physicochemical attributes, through morphological and compositional characterization by advanced spectroscopic and microscopic methodologies, such as scanning transmission electron microscopy (STEM) and energy-dispersive X-ray spectroscopy (EDX). The ensuing characterizations bore witness to the emergence of nanoparticles across all examined sample series (mono-metallic, bi-metallic, and tri-metallic) within the temperature range spanning from 600 °C to 900 °C. The growth in dimensions with the increase in temperatures was evident, particularly the higher thermal points, indicating a substantial evolution in the structure of these electrocatalytic materials.

Fig. 1 shows the comparison between the morphologies of two mono-metallic Fe-based electrocatalysts (Fe 600 and Fe 900) with two different pyrolysis temperatures of 600 °C and 900 °C. In Fe 600, a few nanoparticles of Fe about 50 to 100 nm wide can be seen in (Fig. 1a). When the thermal treatment temperature was turned to 900 °C, a bimodal dimensional dispersion seemed to appear (Fig. 1b): the bigger iron nanoparticles, as seen in Fe 600, and a series of smaller particles, some as tiny as just 5 nm wide. The smaller nanoparticles are forming mainly due to the thermal treatment, and they play an important role in how the electrocatalysts perform.

In the results from the TEM analysis of the Fe–Ni samples which are shown in Fig. 2, some exciting insights have emerged. From the samples pyrolyzed at 600 °C (Fe–Ni 600), a distribution of nanoparticles primarily. Upon examining the

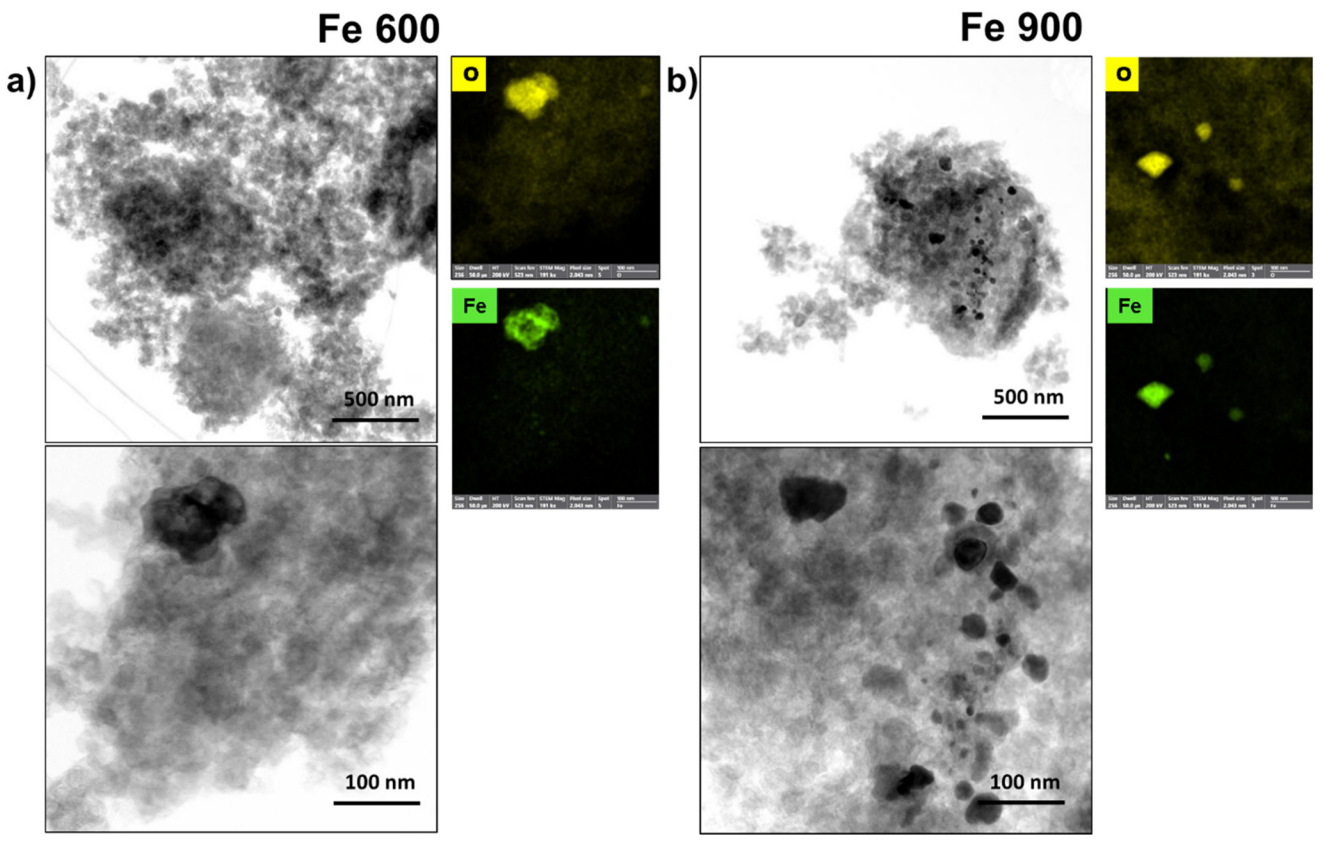


Fig. 1 (a) STEM, and EDX maps at the O, Fe K X-ray K of the Fe 600 and (b) STEM, and EDX maps at the O, Fe X-ray K emissions of the Fe 900.

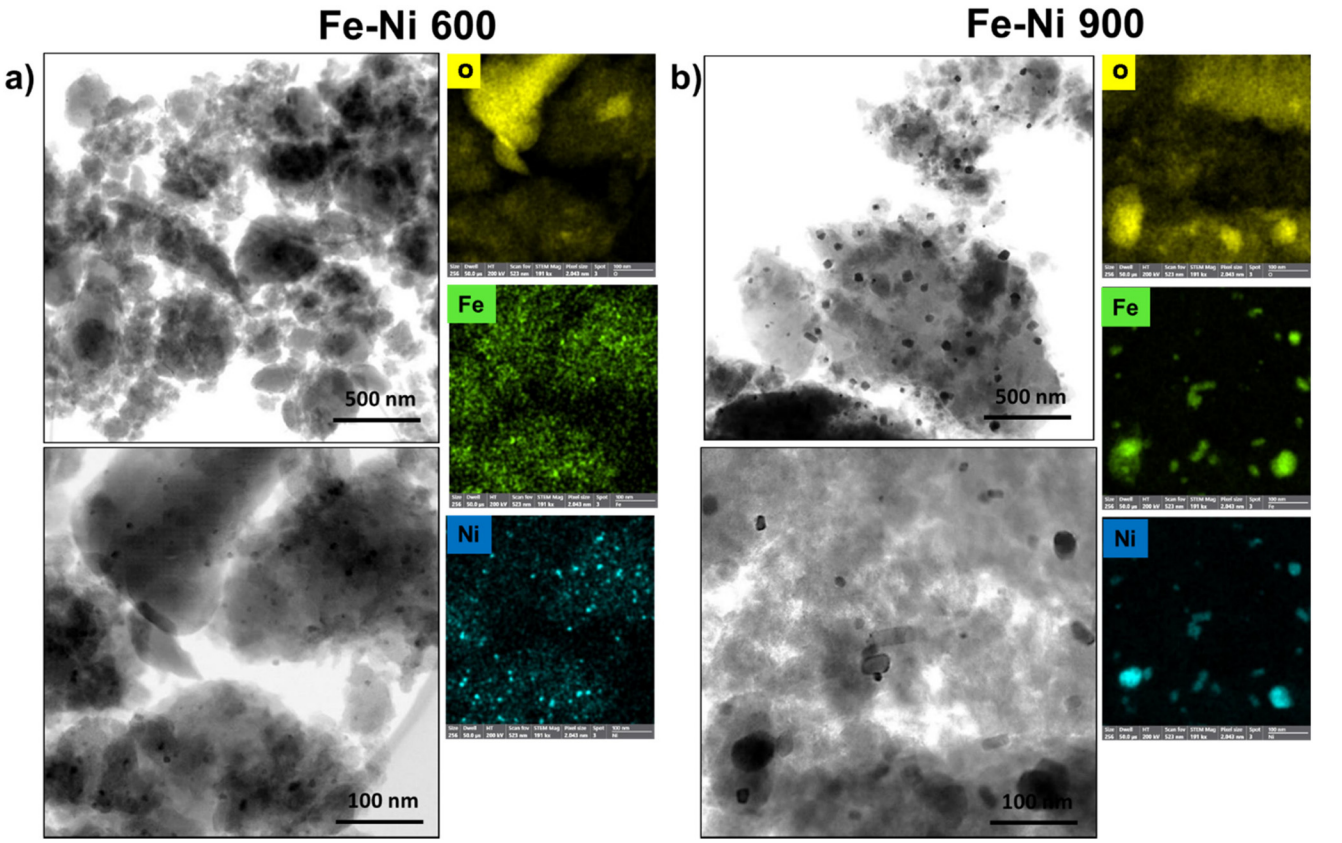


**Fig. 2** (a) STEM, and EDX maps at the O, Fe, Ni K X-ray K of the Fe–Ni 600 and (b) STEM, and EDX maps at the O, Fe, Ni X-ray K emissions of the Fe–Ni 900.

sample exposed to 900 °C (FeNi 900), a growth of the particles till 10–20 nm was noticeable. The composition of the Fe–Ni 900 particles exhibits a bifurcated nature. A fraction of the larger particles appear to constitute a hybrid composition of both iron and nickel. Concurrently, a separate subset of particles (the smaller ones) reports a single-metal composition primarily as phases of $FeO_x$ and $Ni/NiO_x$.

The TEM results related to tri-metallic samples (Fe–Ni–Cu 600 and Fe–Ni–Cu 900) are shown in (Fig. 3). At 600 °C, the examination of the Fe–Ni–Cu samples reveals an absence of nanoparticles. A pattern of segregation between the elements emerges upon transitioning to 900 °C, where two different groups of nanoparticles emerge. In the first group, similar to monometallic samples, metallic Fe atoms and O bond together to form Fe-oxide nanoparticles, while metallic Ni and Cu atoms, bonding together, construct different nanoparticles separate from the Fe-oxide nanoparticles. This implies that, in the presence of Cu atoms, Ni atoms, contrary to Fe–Ni samples, avoid forming an M–M bond with Fe atoms and instead prefer bonding with Cu atoms. This segregation phenomenon, which is not present in each particle, but is evenly distributed adds a layer of complexity to the structural understanding of the Fe–Ni–Cu samples, offering valuable insights into the intricate interactions between these metals in response to thermal changes.

### 2.2. Raman investigation

The Raman spectra on Fe-based electrocatalysts are shown in Fig. 4. The obtained results indicate the presence of carbon. In fact, the usual carbon's signature peaks, such as the D band which is caused by in-plane defects, and imperfections in carbon structures is located at ~1350 $cm^{-1}$. Also, the G band is located at ~1580 $cm^{-1}$ which is related to the $E_{2g2}$ vibration mode of $sp^2$-bonded carbon atoms in graphite with $D_{6h}^4$ crystal symmetry, which can be observed in the spectra.[64–66] Within intravalley double resonance scattering, the other carbon peak, D* band (or $D_2$), which is located at ~1620 $cm^{-1}$, occurs as a result of discontinuity defects that provide the lost momentum needed to satisfy the resonant process.[67–70] Usually, this type of peak appears in very poorly organized carbon structures which are not highly crystallized.[71–74] Also, defects outside the plane of some materials such as tetrahedral carbons, which have atomic layers, are the reason for the existence of $D_3$ band which is located ~1500 $cm^{-1}$.[65,70] In the graphitic carbon, the integrated intensity ratio $I_D/I_G$ is used to characterize the defect quantity and to quantify the graphitization process which is important for electron transfer in electrocatalysis. In other words, the carbon's discontinuities and defects play roles as electrocatalytically active moieties for ORR.[75]

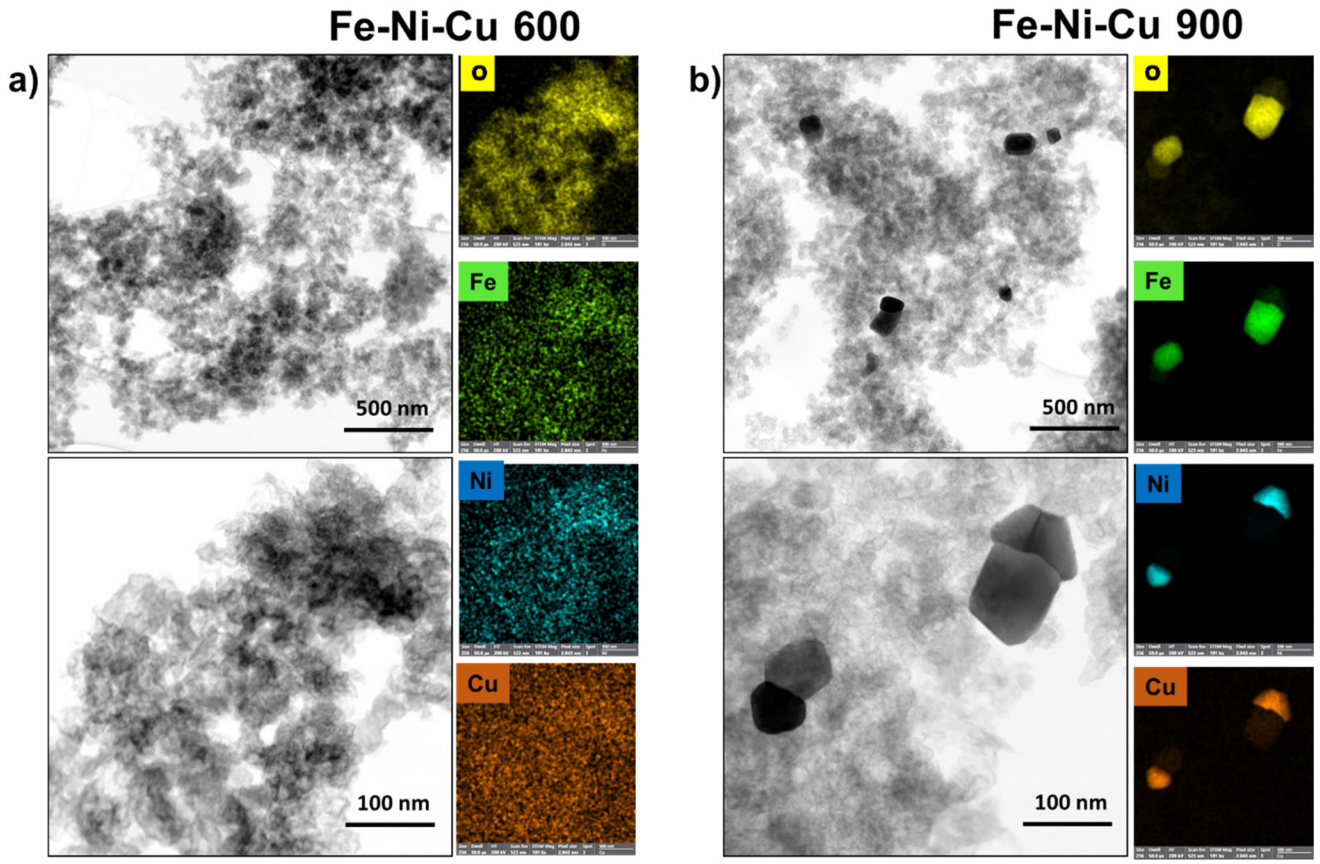


**Fig. 3** (a) STEM, and EDX maps at the O, Fe, Ni, Cu K X-ray K of the Fe–Ni–Cu 600 and (b) STEM, and EDX maps at the O, Fe, Ni, Cu X-ray K emissions of the Fe–Ni–Cu 900.

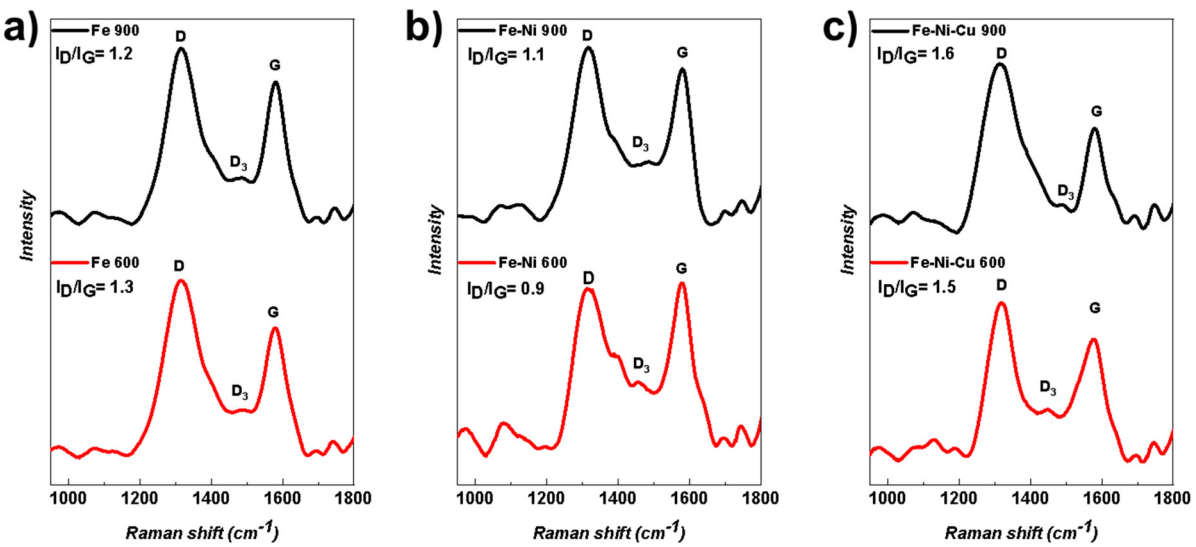


**Fig. 4** Fe-based electrocatalysts Raman spectra with two different functionalization temperatures of 600 °C and 900 °C for (a) Fe, (b) Fe–Ni, (c) Fe–Ni–Cu.

In Fig. 4, a higher degree of graphitization was observable in Fe-based electrocatalysts functionalized at 900 °C compared to the samples with 600 °C functionalization temperature. Notably, variations in pyrolysis temperature result in changes in the $I_D/I_G$ intensity ratio, as an increase in pyrolysis temperature leads to alterations in both the degree of graphitization

 

and the defects in the carbon structure and increase them. Regarding the Fe mono-metallic electrocatalysts (Fe 600 and Fe 900), the $I_D/I_G$ ratio decreased by increasing the pyrolysis temperature which is demonstrated in Fig. 4a. In the bi-metallic (Fe–Ni 600 and Fe–Ni 900) and the tri-metallic (Fe–Ni–Cu 600 and Fe–Ni–Cu 900) (Fig. 4b and c), the $I_D/I_G$ ratio increased by increasing the functionalization temperatures.

### 2.3. XRD results and analysis

Fig. 5 shows the crystallographic features of the as-developed electrocatalysts by using XRD characterization. In all the XRD spectra, the two amorphous carbon broad peaks at 24° (002) and 44° (101), which were caused by the backbone carbon, were recognizable.[76] In the spectra related to the electrocatalysts functionalized at 600 °C, only two broad peaks could be observed indicating no presence of the crystalline phases of the metal(s) of interest. However, it must be noted that some sharp peaks appeared in the XRD spectra of the Fe-based electrocatalysts functionalized at 900 °C. For the Fe 900 electrocatalyst, the peaks of the Fe metal and the Fe oxide were present (Fig. 5a). In the Fe–Ni 900 spectra (Fig. 5b), due to a reduction in wt% of FePc precursor from 30 wt% to 15 wt% (compared to Fe 900), the Fe oxide peaks were not as sharp as the Fe 900 sample; however, the Ni metal peaks were detectable. In the tri-metallic electrocatalysts, Fe–Ni–Cu 900, also Cu metallic XRD peaks were included in (Fig. 5c). These peaks, related to metals and metal oxide, were shown due to the existence of metallic nanoparticles in the samples with higher functionalization temperatures. At 900 °C, the metal atoms form small metallic clusters and nanoparticles.[77,78]

### 2.4. Surface chemistry analysis through XPS

The XPS survey spectra of monometallic (Fe 600 and Fe 900), bimetallic (Fe–Ni 600 and Fe–Ni 900), and trimetallic (Fe–Ni–Cu 600 and Fe–Ni–Cu 900) electrocatalysts are shown in Fig. S1a, b and c,† respectively. The peaks at about 320 eV and 980 eV, not identified in the figures, are related to shake-up lines of C 1s and O KLL signals, respectively. Atomic percentages, derived from survey spectra and displayed in Table S1,† show that the electrocatalysts treated at higher temperatures have a larger content of carbon (C 1s) and a lower amount of both nitrogen (N 1s) and oxygen (O 1s). Carbon percentage ranges from 89.4% in Fe–Ni–Cu 600 and Fe–Ni 600 to 95.7% for Fe 900, while nitrogen percentage ranges from 1.6% for Fe 900 to 4.4% for Fe–Ni 600. The metal atomic percentages (Fe, Ni, and Cu) in all the KJB-supported electrocatalysts are very low with a maximum value of 0.6% as the total metal content in Fe–Ni–Cu 600.

Fig. 6a–c displays XPS spectra related to N 1s deconvolution spectra fitting the signals of imine (397.7 eV), pyridinic-N (398.3 eV), $N_x$–Fe or N–metal (399.1 ± 0.1 eV), pyrrolic-N (400.9 eV), and graphitic-N (402.1 eV) species, as reported in the literature for similar compounds and detailed in Table S2.†[79–84]

All the electrocatalysts treated at 600 °C have a more effective content of N–metal species than samples treated at 900 °C. The pyridinic/pyrrolic ratio is >1 for the samples treated at 600 °C and <1 for the electrocatalysts treated at 900 °C. However, a remarkable error in the relative percentage composition is caused by the low overall atomic percentage, mainly for Fe–Ni–Cu 900 in Fig. 6c.

XPS on carbon (C 1s) speciation is undoubtedly a more relevant investigation useful to match up the different species to ORR activity in alkaline media.[83,84] Fig. 7 shows the deconvoluted peaks corresponding to graphitic carbon at 284.3 eV, secondary carbons such as C–N or C–O at 285.0 eV, $CN_x$ defects at 286.2 eV, C-OH/C-OC at 287.1 eV, C═O at 288 eV and COOH at 289.4 eV. These results are summarized in Table S3.† The electrocatalysts treated at 900 °C have a larger percentage of graphitic carbon than electrocatalysts treated at 600 °C, as found also by Raman spectroscopy. As expected, electrocatalysts treated at 900 °C exhibit a lower relative percentage of C–N defects compared with the corresponding 600 °C-based electrocatalysts.

### 2.5. XAS analysis

Normalized XANES spectra collected on FePc samples are plotted in Fig. 8a. Only FePc at room temperature (RT), treated at 600 °C (Fe 600) and at 900 °C (Fe 900) were analyzed because they showed the best electrocatalytic activity for ORR in alkaline media among the different samples analyzed in

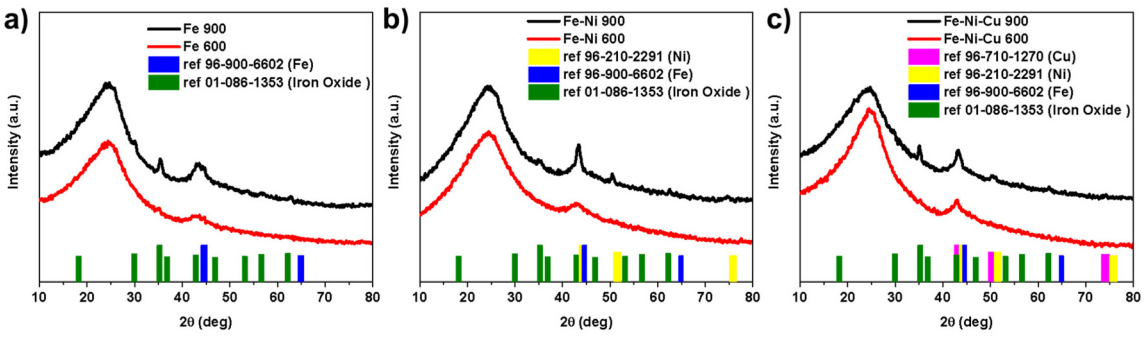


**Fig. 5** Fe-based electrocatalysts XRD spectra at two different 600 °C and 900 °C functionalization temperatures for (a) Fe, (b) Fe–Ni, and (c) Fe–Ni–Cu samples.

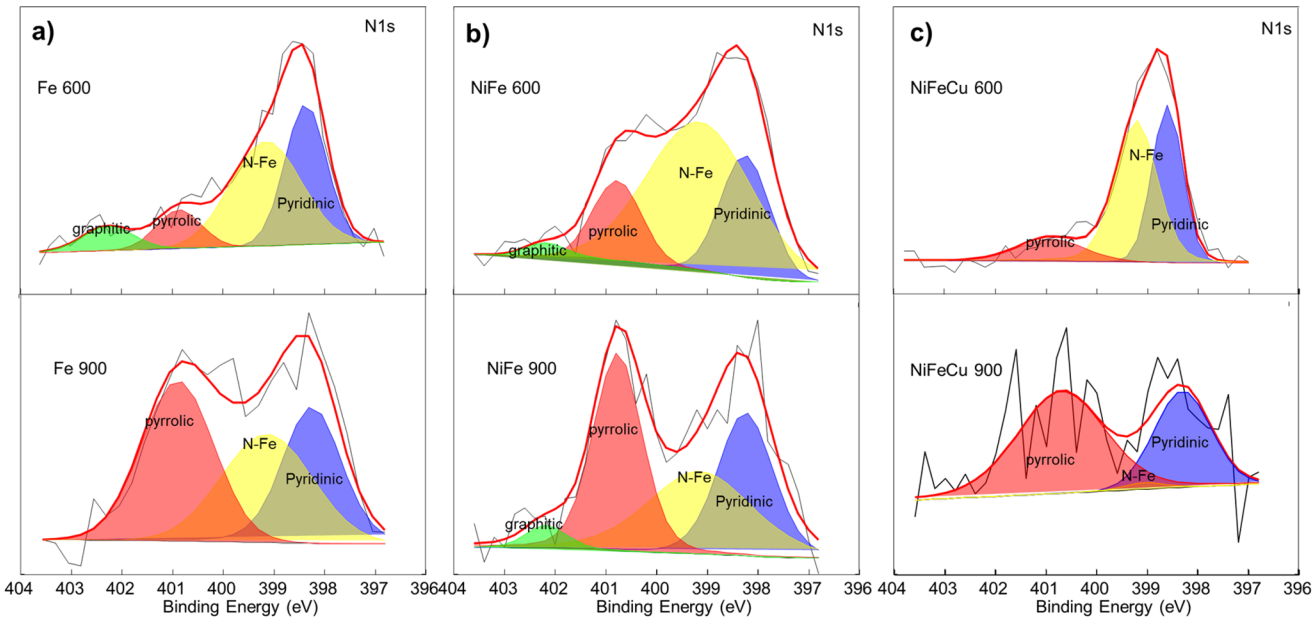


Fig. 6 Comparison of XPS N 1s signal for (a) Fe 600 and Fe 900, (b) Fe–Ni 600 and Fe–Ni 900 and (c) Fe–Ni–Cu 600 and Fe–Ni–Cu 900.

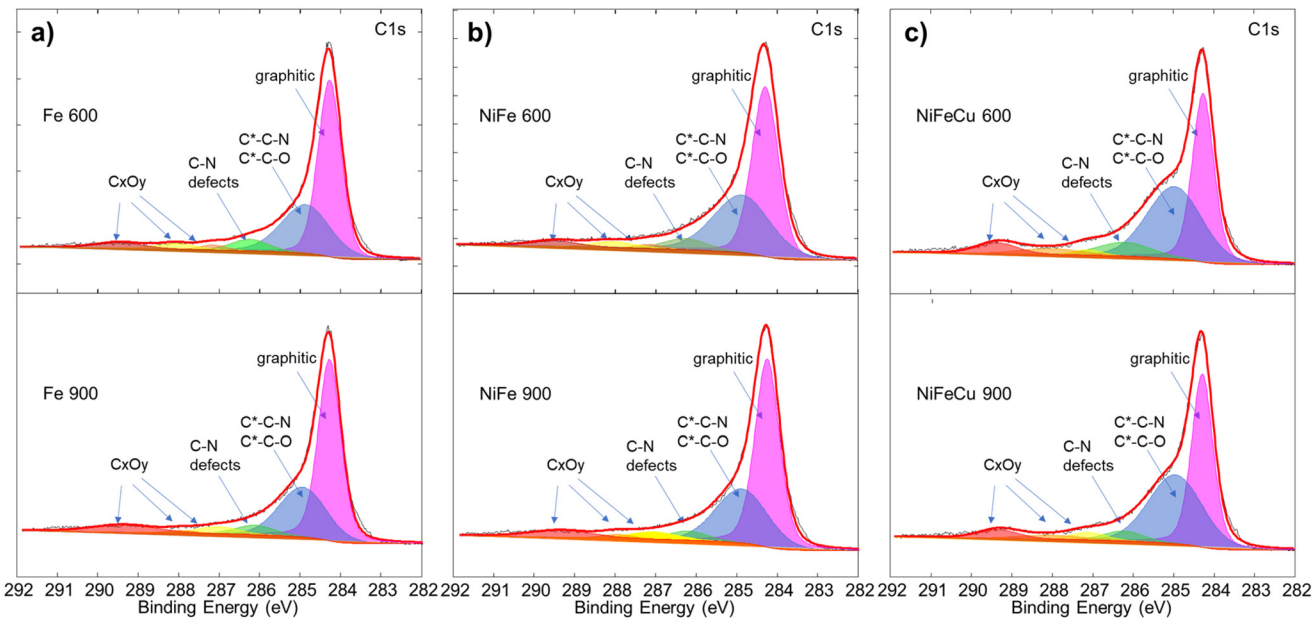


Fig. 7 Comparison of XPS C 1s signal for (a) Fe 600 and Fe 900, (b) Fe–Ni 600 and Fe–Ni 900 and (c) Fe–Ni–Cu 600 and Fe–Ni–Cu 900.

this study (see below). In all spectra, a clearly visible pre-edge peak at about 7114 eV (labeled P in Fig. 8a) which is supposed to originate from the electron transition of 1s → 3d is present and falling in the energy range common to many other $Fe^{3+}$ oxide references, like Magnetite ($Fe_3O_4$), Goethite (FeOOH) and Fe-nitrate ($Fe(NO_3)_3{\cdot}(H_2O)_9$).[85] This fact, together with the edge position, is the first indication of the presence of mainly $Fe^{3+}$. In addition, according to Guo *et al.*, this peak should be relatable to a square-pyramidal structure with a $C_{4v}$ symmetry.[86]

The spectrum collected on the sample treated at 600 °C is generally similar to the untreated one, despite being the only one to have a second pre-edge peak (labeled A in Fig. 8a, around 7118 eV); this peak is compatible with that reported by Chang *et al.* and should relate to 1s → $4p_z$ metal electronic (dipolar) transition, probably involving Fe 2nd neighbors.[85,88]

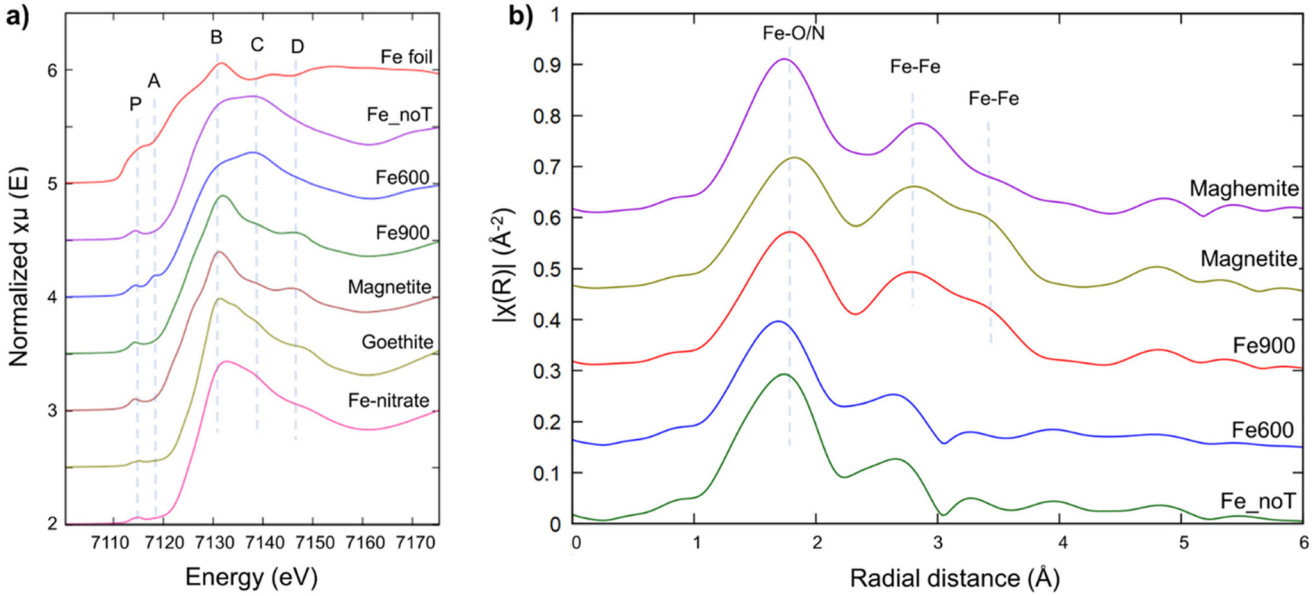


**Fig. 8** (a) Comparison of the Fe K-edge normalized XANES spectra of samples and Fe-bearing reference compounds provided by the XAFS beamline database. Features of the samples were labeled following the same approach of Mirshokraee *et al.*[87] (b) Comparison between the *k*1 Fourier transformed EXAFS spectra (phase corrected) at the Fe K-edge of the samples and magnetite and maghemite ($Fe_3O_4$ and $\gamma$-$Fe_2O_3$, respectively) reference compounds.

The presence of this peak may indicate the presence of Fe coordinated with four nitrogen atoms in the $D_{4h}$ symmetry; however, considering that in 600 °C sample spectrum the two peaks (P and A) coexists, the change of Fe symmetry is anyway only partial.

In addition, the split white line peak visible in both untreated and 600 °C sample data (7130–7140 eV, feature "B" and "C" in Fig. 8a) should indicate the axial coordination of central Fe atom with a big conjugated structure rather than with only O atom.[86] As expected, the spectrum from the sample treated at 900 °C is the most different: the edge position is slightly red-shifted (pointing to more reduced Fe, expected upon heat treatment), the white line is now a single and more intense peak and a new feature appears at around 7146 eV (labeled D in Fig. 8a); all these differences make the spectrum of the 900 °C sample very similar to that of magnetite (Fig. 8a).

XANES spectrum from the sample treated at 900 °C has been also analyzed through Linear Combination Fitting (LCF); a good fit can be achieved using only the spectrum of untreated sample and magnetite, with a percentage of 19% and 81% (±2%), respectively (Fig. S2†).

The pre-edge peaks of data from samples were also analyzed through deconvolution (upon normalization and background removal); the centroid energy positions suggest that iron is present mainly as $Fe^{3+}$, while the integrated intensities of the pre-edge peaks point to an average Fe five-fold coordinated (or a mixture of four-fold and six-fold coordination, as in magnetite). The main change is the intensity of the second pre-edge peak, which is present only in the sample heated at 600 °C (Fig. S3†).

The Fourier-transformed (FT) EXAFS spectra (Fig. 8b) show in all the samples the presence of a first shell composed of Fe–N bonds, at nearly 1.7 Å. This shell is however changing among the samples either in terms of amplitude and bond length, supporting a partial change in the Fe symmetry from untreated sample to the 600 °C (already hypothesized from pre-edge peaks results) despite the long-range order is generally preserved as the second shell of pristine and 600 °C samples are similar. On the contrary (and in agreement with LCF results) the overall structure change in the 900 °C sample, to becomes very similar to that of Magnetite (Fig. 8b).

## 2.6. Oxygen reduction reaction analysis in alkaline media

**2.6.1. Effect of FePc precursor weight percentage (wt%) on the ORR electrochemical performance.** The rotating ring disk electrode (RRDE) measurements were done with a rotation speed of 1600 rpm in oxygen-saturated 0.1 M KOH electrolyte to demonstrate the ORR activity of the Fe-based electrocatalysts. The onset potentials ($E_{on}$) were determined using a current density of −0.1 mA $cm^{-2}$. The measurements were performed at a scan rate of 5 mV $s^{-1}$. In the first step, the ORR of the Fe-based electrocatalysts with different FePc wt% and two different functionalization temperatures of 600 °C and 900 °C were analyzed (Fig. 9). For this measurement, a loading of 0.6 mg $cm^{-2}$ electrocatalyst was deposited for each sample over the glassy carbon electrode disk.

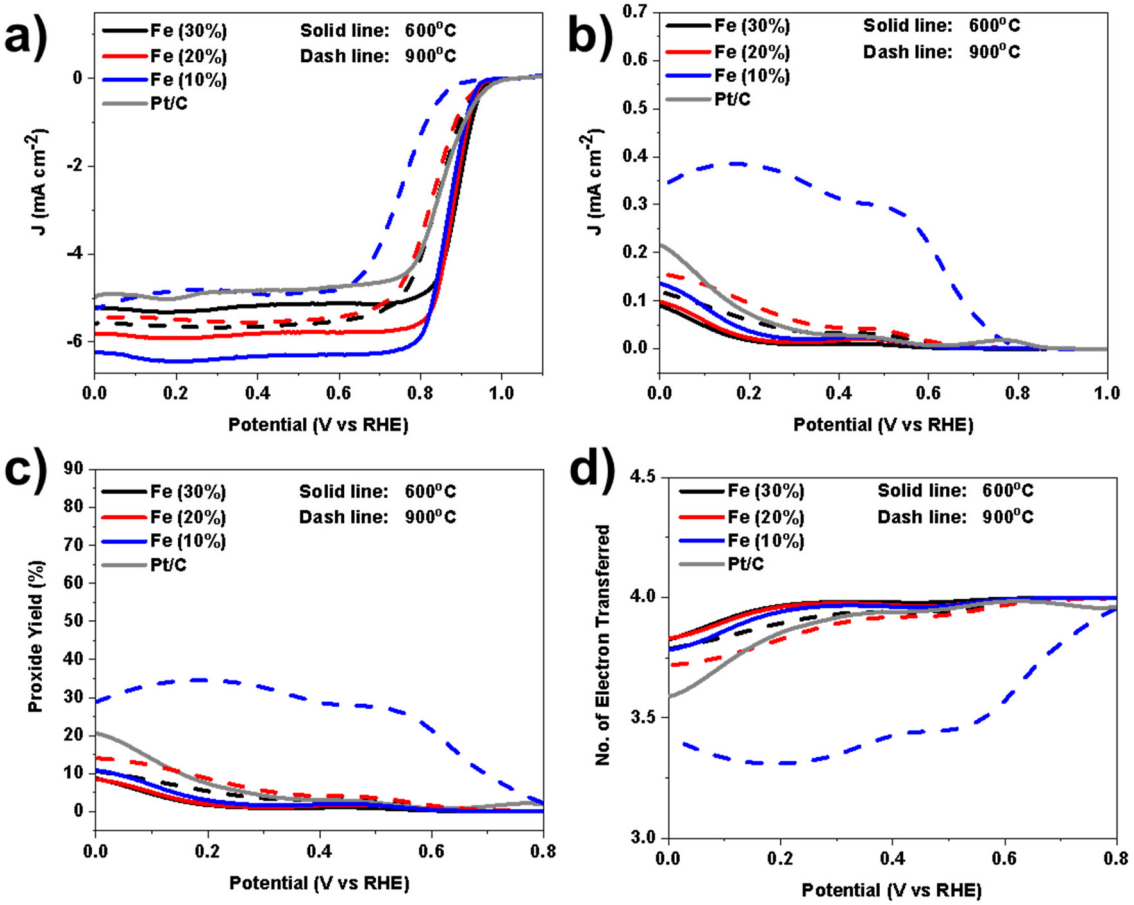


**Fig. 9** The RRDE measurement of the ORR for Fe-based electrocatalysts with different FePc wt% as precursors run at 1600 rpm in 0.1 M KOH. (a) LSV for disk current, (b) ring current, (c) peroxide anion yield, and (d) number of electrons transferred. Pt/C in all plots is the benchmark.

In addition to $E_{on}$, the half-wave potential ($E_{1/2}$) providing information about the kinetics of the ORR process, was estimated by performing a first differential method. Moreover, the limiting current density values are also reported in Table S4.† According to the outcome results (Fig. 9a), the electrocatalysts that underwent a lower temperature during the functionalization (600 °C) showed a higher electrocatalytic activity compared to the same samples functionalized at higher temperatures (900 °C). In another comparison, the Fe-based electrocatalysts with the higher wt% of FePc demonstrated higher activity. The Fe(30%)600 sample showed higher activity, with an $E_{on}$ of 0.96 V (*vs.* RHE) and $E_{1/2}$ of 0.89 V (*vs.* RHE). The Fe (20%)600 catalyst presented values of $E_{on}$ of 0.95 V (*vs.* RHE) and the $E_{1/2}$ of 0.88 V (*vs.* RHE), very close to the Fe(30%)600, indicating that the increase of the FePc from 20 wt% to 30 wt% does not have a significant enhancement.

The next considerable parameters that help to better understand the ORR performance of the Fe-based electrocatalysts are the number of electrons transferred and the peroxide anion produced. An ideal ORR electrocatalyst should have the maximum number of electrons transferred, in this case 4, and therefore lower or no intermediates (peroxide anions) produced. For calculating electron transfer and peroxide anion produced, the ring current is necessary and it is shown in Fig. 9b. It is essential to determine how many electrons are transferred during the ORR for understanding the stoichiometry of the reaction, optimizing energy efficiency, determining reaction kinetics, and designing effective electrocatalysts.[89]

Peroxide is also a product of the ORR, it is generally undesirable during the ORR process for many reasons such as reduction of efficiency, stability, and reaction kinetics. Also, peroxide can cause corrosion of the electrode materials and other components in the ORR system.[90,91] The peroxide anion production is shown in Fig. 9c. Again, the electrocatalysts pyrolyzed at 600 °C showed important results by producing less than 10% peroxide along the potentials investigated. It should be mentioned that there was no noticeable difference in samples functionalized at 600 °C with different FePc wt%. Interestingly, Fe-based electrocatalysts functionalized at 900 °C showed a similar trend to the samples functionalized at 600 °C in the case containing 20 wt% and 30 wt% of Pc precursor. Fe (10%)900 instead, showed higher production of peroxide, up to 35% (Fig. 9c). Identifying the peroxide produced, the number of electrons transferred can be determined. The related electrons transferred for Fe-based electrocatalysts with different wt% of FePc are reported in Fig. 9d. All the electroca-

 

talysts with functionalization temperature of 600 °C had more than 3.75 electrons transferred during the ORR process within the potentials range investigated which is very interesting for this kind of electrocatalysts. The difference in FePc wt% in samples at 600 °C did not have a considerable difference in the number of electrons transferred. In the case of Fe-based electrocatalysts functionalized at 900 °C, Fe (10%)900 showed relatively lower electron transfer capability compared to the other samples. By considering the electron transfer and peroxide anion production, Fe-based electrocatalysts at 600 °C even had better performance compared to Pt/C benchmark electrocatalysts.

The results obtained from these measurements clearly indicate a superior performance of the samples functionalized at 600 °C compared to those functionalized at 900 °C, primarily attributed to differences in their structural characteristics. As revealed by the characterizations conducted in the preceding sections, including XAS, XRD, and TEM, it is evident that at higher temperatures, there is observable nanoparticle nucleation. In contrast, at lower temperatures, the metal is dispersed atomically within the electrocatalyst, resulting in an enhancement of the ORR performance. Moreover, based on the XPS analysis, it was evident that the samples functionalized at 600 °C exhibited a higher amount of N–M and pyridinic active sites (N 1s), in combination with C–N defects and a lower degree of graphitization (C 1s). These active sites were important in improving the ORR activity.[32]

**2.6.2. Mono/bi/tri metallic Fe-based electrocatalysts ORR electrochemical performance.** The RRDE electrochemical measurements were carried out also on mono/bi/tri-metallic Fe-based electrocatalysts, subjected to different functionalization temperatures: 600 °C and 900 °C. The experimental protocol followed the methodology explained in the previous section (Fig. 10). As illustrated in Fig. 10a, the Fe 600 and Fe–Ni–Cu 600 electrodes exhibited the most promising results, with $E_{on}$ values of 0.96 V (*vs.* RHE) and $E_{1/2}$ values of 0.9 V (*vs.* RHE). The comprehensive data, in terms of $E_{on}$, $E_{1/2}$ and $j_{lim}$, are reported in (Table S5†). The results unequivocally demonstrate the superior performance of Fe-based electrocatalysts functionalized at 600 °C, as compared to those functionalized at 900 °C. Moreover, the mono and tri-metallic samples outperformed their bi-metallic counterparts significantly. In fact, the addition of nickel to iron seems to decrease the electrocatalytic activity of the electrocatalysts, both functionalized at 600 °C and 900 °C. Interestingly, the addition of Cu to the Fe–Ni, in the trimetallic mode, improved the performance and

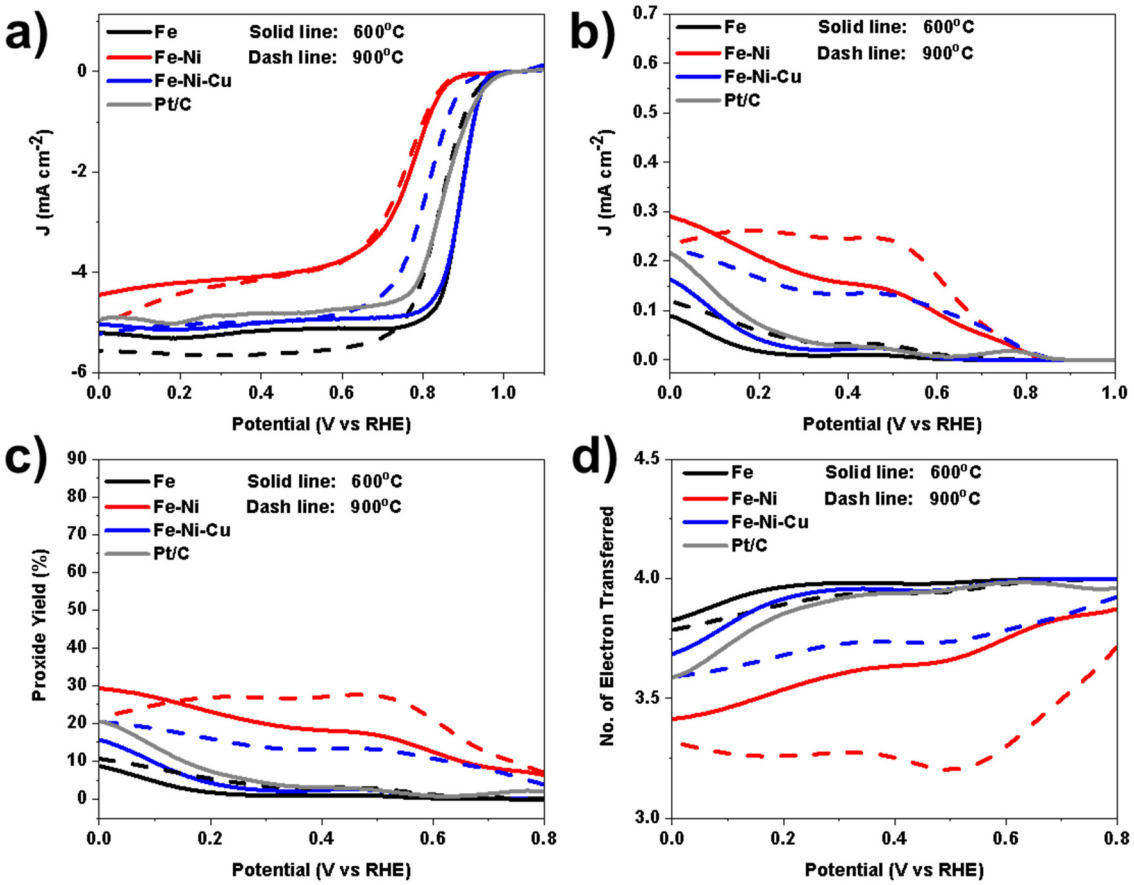


**Fig. 10** The RRDE measurement of the ORR for Fe-based electrocatalysts with different mono/bi/tri-metallic precursors run at 1600 rpm in 0.1 M KOH. (a) LSV for disk current, (b) ring current, (c) peroxide anion yield, and (d) number of electrons transferred. Pt/C in all plots is the benchmark.

showed similar activity compared to Fe 600. Instead, Fe–Ni–Cu 900 had higher activity toward ORR compared to Fe–Ni 900 but still lower compared to Fe 900.

Further supporting evidence can be observed in the ring currents illustrated in Fig. 10b. Concerning anion peroxide production (Fig. 10c), the mono-metallic samples (Fe 600 and Fe 900) stand out with impressively low levels (<10%). Similarly, the tri-metallic sample subjected to thermal treatment at 600 °C (Fe–Ni–Cu 600) shows commendable performance by producing a relatively small amount (<15%) of anion peroxide. However, the tri-metallic sample treated at a higher pyrolysis temperature (Fe–Ni–Cu 900) fails to deliver the same favorable results (<20%). Concerning bimetallic samples, the addition of nickel as a secondary metal increases the peroxide produced.

As illustrated in Fig. 10d, both mono-metallic and tri-metallic samples display a number of electrons transferred during ORR greater than 3.5. This was due to the high electrocatalytic activity and low peroxide production. Remarkably, the samples functionalized at 600 °C consistently exhibit superior performance, even concerning this parameter.

The findings in this section reveal the significance of N–M, pyridinic sites, C–N defects and graphitic C-species in the ORR reaction. Electrocatalysts with a higher abundance of N–M, pyridinic sites and C–N defects, tend to outperform others. In the case of samples subjected to a 900 °C functionalization temperature, most of the metallic atoms combine, forming metallic nanoparticles through M–M bonds. Consequently, this leads to a reduction in N–M sites and a corresponding decrease in ORR activity. Considering the pivotal role of metallic atomic sites, the performance of each type of metallic atom in driving the ORR reaction becomes crucial. Notably, the diminished performance of Fe–Ni 600, compared to Fe 600 and Fe–Ni–Cu 600, can be attributed to its higher content of Ni metal, which is less effective than Fe and Cu in catalyzing the ORR.

Operative stability, particularly in electrocatalysts for fuel cells, is considered a crucial property. An ORR stability assessment for Fe 600 was conducted using an accelerated stability test, involving the execution of 2500 cycles with a scan rate of 50 mV $s^{-1}$.[60,92] Polarization curves were measured at the first cycle and after every 500 cycles, utilizing a scan rate of 5 mV $s^{-1}$, and the results are depicted in (Fig. S4†). No significant changes were observed in $E_{on}$ and $E_{1/2}$ during continuous potential cycling; however, an increase in cycle number revealed a reduction in limiting current density. As the cycles progressed, there was a notable rise in ring current density, accompanied by an enhancement in peroxide anion yield, as indicated by both disk current and ring current results. A comparison between the 2500th and 1st cycles demonstrated a two-time increase in peroxide anion yield. Meanwhile, in the same comparison for the number of electrons transferred, a decrease was observed, declining from 3.7 to 3.5. Overall, noticeable stability can be observed.

### 2.7. Discussion and outlook

The chemical and morphological structures of mono-, bi-, and trimetallic electrocatalysts underwent significant alterations as the pyrolysis temperature was varied from 600 °C to 900 °C, employing diverse techniques for investigation and analysis. A comprehensive examination, utilizing XAS and XRD techniques, yielded invaluable insights into the structural characteristics of the synthesized nanoparticles. At 600 °C, observations from both XAS and XRD unveiled a limited number of nanoparticles, with the metal predominantly coordinated with nitrogen, likely preserving the atomically dispersed Fe–$N_x$ structure of the initial phthalocyanine. Conversely, the analysis at 900 °C revealed a notable increase in nanoparticle population, accompanied by a discernible reduction in the phthalocyanine content (atomically dispersed iron coordinated with nitrogen). The results were corroborated by TEM and EDX characterizations. This intricate correlation between temperature and active site composition underscores the significance of precise thermal control in avoiding or minimizing the presence of nanoparticles within the carbon substrate. It was previously reported that TM-Pc are not stable if they are not subject to a pyrolytic process.[38] This is due to the leaching of the metal and to the lack of integration with the carbon substrate which in turn leads to the washing out of the Pc structure. Therefore, a pyrolytic process is needed to integrate the Pc structure within the carbon matrix.

Furthermore, the investigation of ORR electrocatalysis emphasized the critical role of electrocatalyst composition. This study underscores the necessity of single-atom-based active sites for pursuing an efficient ORR process, highlighting the undesirable nature of nanoparticles-containing electrocatalysts in this context. The introduction of nickel into the electrocatalysts formulation exhibited a dual effect: a dampening impact on the electrocatalytic activity along with an escalation in the intermediate peroxide production, revealing a delicate balance between electrocatalytic efficiency and selectivity. Introducing a third metal into the given electrocatalytic system produced positive results in a specific situation, although it might not work well for all cases. This contrast shows that trimetallic electrocatalysts are quite complex, emphasizing the need to carefully design electrocatalysts to match particular purposes. Overall, the ORR results for Fe 600 and Fe–Ni–Cu 600, with $E_{on}$ values of 0.96 V (*vs.* RHE) and $E_{1/2}$ values of 0.9 V (*vs.* RHE), exhibited intriguing performance compared to similar electrocatalysts reported in previous related articles (Table S6†).[38,56–58,63,93–96]

Looking at the bigger picture, the prevailing preference for bimetallic electrocatalysts incorporating iron (Fe) as a catalytic component emerged as a general trend. It's important to note that adding extra metals to the mix proved to be a multifaceted decision, with its benefits not being universally consistent. This shows that it needs to be carefully thought about what metals should be used in the electrocatalysts, depending on what they're trying to do. Overall, being reminded of these results, it is advisable to exercise thoughtfulness when selecting which metals to employ in an electrocatalyst, particularly when considering their alignment with the specific process being undertaken.

This study utilized precursors that are easy to find and are widely commercially available named carbon black and TM

 

phthalocyanine. This study explores the complex equilibrium between maintaining atomically dispersed transition metals coordinated with nitrogen and creating nanoparticles which are crucial for the correct designing of electrocatalysts, and their operations for ORR especially in bi and tri-metallic electrocatalysts. By combining advanced methods of studying Fe-based electrocatalysts and thoroughly grasping the intricacies, electrocatalysts that are most effective for ORR can be developed. The addition of a second or third metal is not always beneficial as highlighted in this study.

Thus, pursuing comprehensive research into the role of secondary TM introductions, the influence of the choice of TM and concentration relationships along with pyrolysis conditions is necessary to elucidate the prevailing discrepancies, particularly in the case of bi- and tri-metallic electrocatalysts. Consequently, prospective endeavors will be made in this regard to enrich the existing knowledge with the true picture and complete understanding of the performance evolution.

# 3. Conclusions

In this work, the Fe-based electrocatalysts with mono/bi/tri-metallic compositions were created by mixing the necessary TM-Pc with conductive carbon support and subjecting them to controlled thermal treatment in a specific environment and at a particular temperature (600 °C and 900 °C). These electrocatalysts were characterized for their ORR electrocatalytic activity in alkaline media. Increasing the Fe–Pc weight percentage from 10% to 30% improved ORR activity, but the enhancement was not significant. The study involves a comprehensive analysis of synthesized nanoparticles using a variety of techniques such as XAS, TEM and XRD, which yield insights into their structural characteristics. It was observed that at 600 °C, a limited number of nanoparticles and predominance of Pc was present, while at 900 °C, the nanoparticle population increased, but the Pc content decreased. Then, when comparing mono/bi/tri-metallic samples with different functionalization temperatures, it becomes evident that electrocatalysts at 600 °C outperform the same electrocatalysts at 900 °C. The Fe 600 and Fe–Ni–Cu 600 variants, with $E_{on}$ = 0.96 V *vs.* RHE and $E_{1/2}$ = 0.9 V *vs.* RHE, exhibit the best electrocatalytic activity in this context. Moreover, it's worth noting that Fe 600 generates a lower quantity of intermediate products.

# 4. Experimental section

## 4.1. Materials

Ketjen Black 600 (KJB) was used as the carbon support to synthesize the ORR electrocatalyst. KJB was used due to its high surface area, electrical conductivity and commercial availability. KJB purchased from Nanografi Nano Technology (Turkey). Potassium hydroxide (KOH) with a purity of 99.0%, utilized in the preparation of the 0.1 M KOH solution, as well as Nafion® 5 wt% hydro-alcoholic solutions employed for ink formulation were procured from Sigma-Aldrich. Nickel(II) phthalocyanine (NiPc, with the chemical formula $C_{32}H_{16}N_8Ni$), iron(II) phthalocyanine (FePc, with the chemical formula $C_{32}H_{16}N_8Fe$), and Copper(II) phthalocyanine (CuPc, with the chemical formula $C_{32}H_{16}N_8Cu$) were purchased from Acros Organics. The experiments were conducted using ultrapure deionized water, obtained from a Millipore Milli-Q system, with a resistivity exceeding 18 MΩ cm. Argon (Ar) and Nitrogen (N) gases were employed in pyrolysis and electrochemical measurements, both possessing ultra-high purity characteristics.

## 4.2. Synthesis

The main synthesis approach in this work was thermal treatment at high temperatures to prepare the electrocatalyst integrating the metallorganic molecule (Pc in this case) within the porous carbon acting as a backbone.[87] At the first step, to homogeneously mix the metal phthalocyanine of choice (FePc, NiPc, and CuPc) with KJ-Black carbon, a high-energy ball miller ($E_{max}$ Retsch) with a rotation rate of 400 rpm was used for 20 min. The next step was the functionalization of the mixed samples through a thermal treatment at two different 600 °C and 900 °C temperatures in the controlled Ar gas atmosphere (UHP Ar at 100 $cm^3$ $min^{-1}$). The heating rate of the increasing and decreasing temperature ramp before and after the 1-hour dwell time was 5 °C $min^{-1}$. For the first part of the experiment, the different weight percentages (wt%) of the FePc (10, 20, and 30 wt%) were added to carbon and functionalized. In the following Table 1, the functionalized samples with different FePc wt% are demonstrated.

Then, several Fe-based combinations of TM-Pc were used to synthesize the different electrocatalysts. The mixture of KJB with (30 wt%) FePc as monometallic, (15 wt%) FePc and (15 wt%) NiPc as bimetallic, and (10 wt%) FePc, (10 wt%) NiPc and (10 wt%) CuPc as tri-metallic electrocatalysts. Also, in this case, two temperatures were used, 600 °C and 900 °C, respectively. The list of these Fe-based electrocatalysts is shown in Table 2.

## 4.3. Materials advanced characterizations

**4.3.1. TEM imaging.** High-resolution transmission electron microscopy (HRTEM) imaging was performed using a Thermofisher Talos F200X G2 instrument. The imaging

**Table 1** Acronym of the electrocatalysts studied and the synthesis steps are done for a different wt% of the FePc

| Sample | Mix with TM-Pc Fe Pc | Functionalization 600 °C | Functionalization 900 °C |
|---|---|---|---|
| Fe (10%) 600 | 10 wt% | X | |
| Fe (10%) 900 | 10 wt% | | X |
| Fe (20%) 600 | 20 wt% | X | |
| Fe (20%) 900 | 20 wt% | | X |
| Fe (30%) 600 | 30 wt% | X | |
| Fe (30%) 900 | 30 wt% | | X |

Table 2 The list of the samples with the different Fe-based combinations

| | Mix with metal-Pc | | | Functionalization | |
|---|---|---|---|---|---|
| Sample | Fe Pc | Ni Pc | Cu Pc | 600 °C | 900 °C |
| Fe 600 | 30 wt% | | | ■ | |
| Fe 900 | 30 wt% | | | | ■ |
| Fe–Ni 600 | 15 wt% | 15 wt% | | ■ | |
| Fe–Ni 900 | 15 wt% | 15 wt% | | | ■ |
| Fe–Ni–Cu 600 | 10 wt% | 10 wt% | 10 wt% | ■ | |
| Fe–Ni–Cu 900 | 10 wt% | 10 wt% | 10 wt% | | ■ |

process utilized an acceleration voltage of 200 kV and a resolution of 4096 × 4096 pixels, without employing any objective apertures. For capturing high-angle annular dark-field (HAADF) images, an annular scanning transmission electron microscopy (STEM) detector was utilized, with a convergent beam set at an angle of 10.5 mrad. Furthermore, energy dispersive X-ray Analysis (EDX) maps which were acquired with a collection angle of 0.7 srad, were collected using Super X spectrometers equipped with silicon drift detectors, each spanning an area of 30 $mm^2$.

**4.3.2. Raman instrumentation and measurement.** The Jasco Ventuno μ-Raman system utilized in the experiment features a He–Ne laser that has a wavelength of 632.8 nm and a power density of 6 kW $cm^{-2}$. The device is also equipped with a Peltier-cooled charge-coupled device (CCD) camera that operates at a temperature of −50 °C. To calibrate the system, a single crystal Si sample was used as the reference sample, with a domain peak located at 520.65 $cm^{-1}$.

**4.3.3. X-ray diffraction (XRD) analysis.** X-ray diffraction (XRD, Rigaku Miniflex 600) was done using a copper source. XRD measurements were performed over powder samples varying the angle range between 10° and 90°. The variation step was 0.020°. The scanning speed was scanning speed of 1.000° per min.

**4.3.4. X-ray photoelectron spectroscopy (XPS).** X-ray photoelectron spectroscopy (XPS), Physical Electronics (PHI) 5800-01, was employed to determine the atomic composition, from survey spectra, and the speciation of N 1s and C 1s, from deconvolution spectra. The X-ray source was the monochromatic $Alk_\alpha$ at a power of 350 W, as previously reported.[97–99] XPS data were processed with MultiPak V6.1A software linked to the MatLab server, and the data were discussed while keeping into account similar M–N–C electrocatalysts reported in the literature.[79–84]

**4.3.5. X-ray absorption spectroscopy (XAS).** Fe K-edge XAS spectra were collected at the XAFS beamline (ELETTRA, Trieste, Italy) in transmission mode using a fixed exit Si (111) monochromator.[100] For all the samples, energy calibration was accomplished by collecting simultaneously a reference spectrum of a Fe metal foil placed in a second experimental chamber after the sample and after the I1 ionization chamber, with the position of the first inflection point taken at 7112.0 eV.

All spectra were collected at room temperature with a variable energy step as a function of the energy: a large step (5 eV) in the first 200 eV of the spectrum, a smaller step (0.2 eV) in the XANES region and a *k*-constant step of 0.03 $Å^{-1}$ in the EXAFS region. For each sample, 3 spectra have been collected and merged in order to increase the statistic.

The XANES spectra of samples and model compounds were then eventually normalized with respect to the atomic background of the curve using the Athena software.[101] Some normalized XANES spectra were analyzed through linear combination fitting (LCF) of spectra from model compounds (provided by the beamline database), using the Athena software.

The pre-edge peaks have been fit using the package lmfit (on Python 3.10). The region around the pre-peak has been fit in two steps: (I) a first fit of the background, considering only the point around the pre-edge peaks, employing a linear and an arctangent function; (II) a fit of the pre-peaks employing 5 pseudo-Voight functions, with a fraction of 0.5 and an FWHM of 1.5 eV, to reduce the number of parameters. During the second fit, the background parameters have been adjusted allowing the fit value to change around an interval of $\pm 1.5\sigma$, where $\sigma$ is the uncertainty calculated for each parameter of the background. The pre-edge centroid has been calculated as the weighted mean of the first three pre-edge peaks centers, weighted for their intensity.

EXAFS signals for qualitative comparison were extracted using Athena and Fourier transformed with an Hanning window in the *k* range 2.5–10.5 $Å^{-1}$.

### 4.4. Electrochemical characterizations during oxygen reduction reaction (ORR)

For measuring the ORR performance of the developed electrocatalysts, three electrodes method with a rotating ring disk electrode (RRDE) approach was performed. A Pine WaveVortex RDE system coupled with a Pine bipotentiostat equipped with a working electrode which has the glassy carbon disk and the platinum ring geometric area of 0.2376 $cm^2$ and 0.2356 $cm^2$, respectively. A graphite rod and a saturated calomel electrode (SCE) were used as counter and reference electrodes, respectively. The experiments were run in 0.1 M KOH alkaline solution, using a rotation speed of 1600 rpm for the working electrode. An oxygen-saturated solution was obtained in all measurement processes by fluxing oxygen gas into the electrolyte solution. As reported previously, 5 mg of electrocatalyst was mixed with 985 mL of isopropanol and 15 mL of 5 wt% Nafion® D-520 ionomer solution to prepare the inks.[60,102,103] After ink preparation, it was deposited using a micropipette over the glassy carbon disk acting as the working electrode. Generally, in electrochemical measurement of ORR in alkaline media the potential scan range is between 1.2 and 0 V *vs.* RHE. The following equation (eqn (1)) was used to convert all the measured potentials to potential *versus* reversible hydrogen electrode (RHE).

$$E_{RHE} = E_{ref} + 0.059 \cdot pH + E^{\circ}_{ref} \quad (1)$$

In (eqn (1)), $E_{ref}$ is the measured working potential *versus* the reference electrode, $E^{\circ}_{ref}$ is the potential of the reference

 

electrode with respect to the standard hydrogen electrode at 25 °C (0.241 V for SCE). It must be mentioned that during the experiments, the ring potential was fixed at 1.2 V *vs.* RHE. Then by considering the following equations, we used the currents generated by the disk ($I_d$) and by the ring ($I_r$) to calculate electrons transferred ($n$) (eqn (2)), and hydrogen peroxide emitted (eqn (3)).

$$n = \frac{4 \times I_d}{I_d + \frac{I_r}{N}}[\mathrm{nr}] \quad (2)$$

$$H_2O_2 = \frac{200 \times \frac{I_r}{N}}{I_d + \frac{I_r}{N}}[\%] \quad (3)$$

In (eqn (2)) and (eqn (3)), $N$ is the collection efficiency that was 0.38 as reported by the supplier and checked in-house. Besides electrons transferred ($n$) and hydrogen peroxide emission, the onset potential ($E_{on}$) which generally is evaluated by recording the potential generated at a current density of 0.1 mA $cm^{-2}$ in a steady-state measurement, and the half-wave potential ($E_{1/2}$) are used to characterizing the ORR electrocatalyst activity.[104] The $E_{1/2}$ is the potential where half of the maximum current density in the polarization curve is measured.

## Conflicts of interest

There are no conflicts to declare.

## Acknowledgements

S. A. M. acknowledges a Ph.D. scholarship on Green Issues from action IV.5 of the PON Research and Innovation 2014–2020 "Education and research for recovery – REACT-EU" program. C. S. would like to thank the support from ENEA – UNIMIB agreement (Procedure 1.1.3 PNRR POR H2). C. S. would like to acknowledge the Ministry of Foreign Affairs and International Cooperation – Directorate General for Cultural and Economic Promotion and Innovation (Italian Republic) within the bilateral project Italy-Israel (WE-CAT). V. B. and A. L. thank the Italian ministry MUR for funding through the FISR 2019 project AMPERE (FISR2019_01294). The beamtime at the XAFS beamline of Elettra was provided through proposal 20220263 and scheduled in December 2022.

## References

1 D. A. Cullen, K. Neyerlin, R. K. Ahluwalia, R. Mukundan, K. L. More, R. L. Borup, A. Z. Weber, D. J. Myers and A. Kusoglu, *Nat. Energy*, 2021, **6**, 462–474.
2 A. Majumdar, J. M. Deutch, R. S. Prasher and T. P. Griffin, *Joule*, 2021, **5**, 1905–1908.
3 M. Muhyuddin, G. Tseberlidis, M. Acciarri, O. Lori, M. D'Arienzo, M. Cavallini, P. Atanassov, L. Elbaz, A. Lavacchi and C. Santoro, *J. Energy Chem.*, 2023, **87**, 256–285.
4 J. Lindorfer, D. C. Rosenfeld and H. Böhm, in *Future energy*, Elsevier, 2020, pp. 495–517.
5 J. Hyun and H.-T. Kim, *Energy Environ. Sci.*, 2023, 5633–5662.
6 Z. Miao, S. Li, C. Priest, T. Wang, G. Wu and Q. Li, *Adv. Mater.*, 2022, **34**, 2200595.
7 M. M. Hossen, M. S. Hasan, M. R. I. Sardar, J. B. Haider, K. Tammeveski and P. Atanassov, *Appl. Catal., B*, 2023, **325**, 121733.
8 X. Ge, A. Sumboja, D. Wuu, T. An, B. Li, F. T. Goh, T. A. Hor, Y. Zong and Z. Liu, *ACS Catal.*, 2015, **5**, 4643–4667.
9 H. A. Firouzjaie and W. E. Mustain, *Journal*, 2019, **10**, 225–234.
10 Y. He, S. Liu, C. Priest, Q. Shi and G. Wu, *Chem. Soc. Rev.*, 2020, **49**, 3484–3524.
11 B. Wu, T. Sun, Y. You, H. Meng, D. M. Morales, M. Lounasvuori, A. Beheshti Askari, L. Jiang, F. Zeng and B. Hu, *Angew. Chem., Int. Ed.*, 2023, e202219188.
12 W. Wang, Q. Jia, S. Mukerjee and S. Chen, *ACS Catal.*, 2019, **9**, 10126–10141.
13 M. X. Chen, L. Tong and H. W. Liang, *Chem. – Eur. J.*, 2021, **27**, 145–157.
14 Q. Zhang and J. Guan, *J. Power Sources*, 2020, **471**, 228446.
15 S. Sultan, J. N. Tiwari, A. N. Singh, S. Zhumagali, M. Ha, C. W. Myung, P. Thangavel and K. S. Kim, *Adv. Energy Mater.*, 2019, **9**, 1900624.
16 K. Artyushkova, A. Serov, S. Rojas-Carbonell and P. Atanassov, *J. Phys. Chem. C*, 2015, **119**, 25917–25928.
17 K. Singh, F. Razmjooei and J.-S. Yu, *J. Mater. Chem. A*, 2017, **5**, 20095–20119.
18 M. Muhyuddin, P. Mustarelli and C. Santoro, *ChemSusChem*, 2021, **14**, 3785–3800.
19 R. Sgarbi, K. Kumar, F. Jaouen, A. Zitolo, E. A. Ticianelli and F. Maillard, *J. Solid State Electrochem.*, 2021, **25**, 45–56.
20 Y. Meng, X. Huang, H. Lin, P. Zhang, Q. Gao and W. Li, *Front. Chem.*, 2019, **7**, 759.
21 S. Liu, C. Li, M. J. Zachman, Y. Zeng, H. Yu, B. Li, M. Wang, J. Braaten, J. Liu and H. M. Meyer III, *Nat. Energy*, 2022, **7**, 652–663.
22 J. Wang, Y.-C. Huang, Y. Wang, H. Deng, Y. Shi, D. Wei, M. Li, C.-L. Dong, H. Jin and S. S. Mao, *ACS Catal.*, 2023, **13**, 2374–2385.
23 X. Zhang, L. Truong-Phuoc, T. Asset, S. Pronkin and C. Pham-Huu, *ACS Catal.*, 2022, **12**, 13853–13875.
24 N. Zion, L. Peles-Strahl, A. Friedman, D. A. Cullen and L. Elbaz, *ACS Appl. Energy Mater.*, 2022, **5**, 7997–8003.
25 H. C. Honig and L. Elbaz, *ChemElectroChem*, 2023, **10**, e202300042.
26 L. Peles-Strahl, Y. Persky and L. Elbaz, *SusMat*, 2023, **3**, 44–57.
27 Y. Persky, Y. Yurko, R. Z. Snitkoff-Sol, N. Zion and L. Elbaz, *Nanoscale*, 2024, **16**, 438–446.

28 Y. Persky, Ł. Kielesiński, S. N. Reddy, N. Zion, A. Friedman, H. C. Honig, B. Koszarna, M. J. Zachman, I. Grinberg and D. T. Gryko, *ACS Catal.*, 2023, **13**, 11012–11022.
29 I. Matanovic, K. Artyushkova, M. B. Strand, M. J. Dzara, S. Pylypenko and P. Atanassov, *J. Phys. Chem. C*, 2016, **120**, 29225–29232.
30 S. Rojas-Carbonell, K. Artyushkova, A. Serov, C. Santoro, I. Matanovic and P. Atanassov, *ACS Catal.*, 2018, **8**, 3041–3053.
31 I. Matanovic, K. Artyushkova and P. Atanassov, *Curr. Opin. Electrochem.*, 2018, **9**, 137–144.
32 T. Asset and P. Atanassov, *Joule*, 2020, **4**, 33–44.
33 U. Kramm, I. Abs-Wurmbach, I. Herrmann-Geppert, J. Radnik, S. Fiechter and P. Bogdanoff, *J. Electrochem. Soc.*, 2010, **158**, B69.
34 U. I. Koslowski, I. Abs-Wurmbach, S. Fiechter and P. Bogdanoff, *J. Phys. Chem. C*, 2008, **112**, 15356–15366.
35 D. Guo, R. Shibuya, C. Akiba, S. Saji, T. Kondo and J. Nakamura, *Science*, 2016, **351**, 361–365.
36 L. Lai, J. R. Potts, D. Zhan, L. Wang, C. K. Poh, C. Tang, H. Gong, Z. Shen, J. Lin and R. S. Ruoff, *Energy Environ. Sci.*, 2012, **5**, 7936–7942.
37 Z.-Y. Mei, S. Cai, G. Zhao, X. Zou, Y. Fu, J. Jiang, Q. An, M. Li, T. Liu and H. Guo, *Chem. Eng. J.*, 2022, **430**, 132691.
38 M. A. C. De Oliveira, V. C. Ficca, R. Gokhale, C. Santoro, B. Mecheri, A. D'epifanio, S. Licoccia and P. Atanassov, *J. Solid State Electrochem.*, 2021, **25**, 93–104.
39 Z. Zhang, S. Yang, M. Dou, H. Liu, L. Gu and F. Wang, *RSC Adv.*, 2016, **6**, 67049–67056.
40 S. Yang, Y. Yu, X. Gao, Z. Zhang and F. Wang, *Chem. Soc. Rev.*, 2021, **50**, 12985–13011.
41 M. Musilova, J. Mrha and J. Jindra, *J. Appl. Electrochem.*, 1973, **3**, 213–218.
42 V. Bagotzky, M. Tarasevich, K. Radyushkina, O. Levina and S. Andrusyova, *J. Power Sources*, 1978, **2**, 233–240.
43 M. Muhyuddin, E. Berretti, S. A. Mirshokraee, J. Orsilli, R. Lorenzi, L. Capozzoli, F. D'Acapito, E. Murphy, S. Guo and P. Atanassov, *Appl. Catal., B*, 2024, **343**, 123515.
44 H. R. Litkohi, A. Bahari and M. P. Gatabi, *Int. J. Hydrogen Energy*, 2020, **45**, 23543–23556.
45 B. Li and S. H. Chan, *Int. J. Hydrogen Energy*, 2013, **38**, 3338–3345.
46 D. Liu, L. Tao, D. Yan, Y. Zou and S. Wang, *ChemElectroChem*, 2018, **5**, 1775–1785.
47 G. Bampos, S. Bebelis, D. I. Kondarides and X. Verykios, *Top. Catal.*, 2017, **60**, 1260–1273.
48 X. Deng, S. Imhanria, Y. Sun, M. Zhang, Y. Cheng and W. Wang, *J. Environ. Chem. Eng.*, 2022, **10**, 108052.
49 M. Neergat, V. Gunasekar and R. Rahul, *J. Electroanal. Chem.*, 2011, **658**, 25–32.
50 N. Xue, Y. Zhang, C. Wang, X. Xue, D. Ouyang, H. Zhu and J. Yin, *Int. J. Hydrogen Energy*, 2022, **47**, 33979–33987.
51 J. Hu, C. Zhang, M. Sun, Q. Qi, S. Luo, H. Song, J. Xiao, B. Huang, M. K. Leung and Y. Zhang, *Nano Res.*, 2022, **15**, 4950–4957.
52 Y. Kumar, E. Kibena-Põldsepp, M. Mooste, J. Kozlova, A. Kikas, J. Aruväli, M. Käärik, V. Kisand, J. Leis and A. Tamm, *ChemElectroChem*, 2022, **9**, e202200717.
53 F. Luo, S. Wagner, I. Onishi, S. Selve, S. Li, W. Ju, H. Wang, J. Steinberg, A. Thomas and U. I. Kramm, *Chem. Sci.*, 2021, **12**, 384–396.
54 M. Lüsi, H. Erikson, H.-M. Piirsoo, P. Paiste, J. Aruväli, A. Kikas, V. Kisand, A. Tamm and K. Tammeveski, *J. Electroanal. Chem.*, 2022, **917**, 116391.
55 A. Serov, M. H. Robson, M. Smolnik and P. Atanassov, *Electrochim. Acta*, 2012, **80**, 213–218.
56 S. Wang, Z. Li, W. Duan, P. Sun, J. Wang, Q. Liu, L. Zhang and Y. Zhuang, *J. Energy Chem.*, 2023, **86**, 41–53.
57 H. Li and Z. Sui, *New J. Chem.*, 2019, **43**, 17963–17973.
58 X. Wang, Y. Liu, Y. Wang, R. Ren, H. Chen, Z. Jiang and Q. He, *ChemElectroChem*, 2018, **5**, 3478–3485.
59 Y. Kumar, E. Kibena-Põldsepp, J. Kozlova, M. Rahn, A. Treshchalov, A. Kikas, V. Kisand, J. Aruvali, A. Tamm and J. C. Douglin, *ACS Appl. Mater. Interfaces*, 2021, **13**, 41507–41516.
60 M. Muhyuddin, A. Friedman, F. Poli, E. Petri, H. Honig, F. Basile, A. Fasolini, R. Lorenzi, E. Berretti and M. Bellini, *J. Power Sources*, 2023, **556**, 232416.
61 A. Serov, M. H. Robson, M. Smolnik and P. Atanassov, *Electrochim. Acta*, 2013, **109**, 433–439.
62 Q. Liu, S. Cao, Y. Fu, Y. Guo and Y. Qiu, *J. Electroanal. Chem.*, 2018, **813**, 52–57.
63 K. Muuli, R. Kumar, M. Mooste, V. Gudkova, A. Treshchalov, H.-M. Piirsoo, A. Kikas, J. Aruväli, V. Kisand and A. Tamm, *Materials*, 2023, **16**, 4626.
64 D. Testa, G. Zuccante, M. Muhyuddin, R. Landone, A. Scommegna, R. Lorenzi, M. Acciarri, E. Petri, F. Soavi and L. Poggini, *Catalysts*, 2023, **13**, 635.
65 C. Beny-Bassez and J. Rouzaud, *Scanning Electron Microsc.*, 1984, **1985**, 11.
66 A. C. Ferrari, J. C. Meyer, V. Scardaci, C. Casiraghi, M. Lazzeri, F. Mauri, S. Piscanec, D. Jiang, K. S. Novoselov and S. Roth, *Phys. Rev. Lett.*, 2006, **97**, 187401.
67 A. C. Ferrari, *Solid State Commun.*, 2007, **143**, 47–57.
68 L. G. Cançado, A. Jorio, E. M. Ferreira, F. Stavale, C. A. Achete, R. B. Capaz, M. V. D. O. Moutinho, A. Lombardo, T. Kulmala and A. C. Ferrari, *Nano Lett.*, 2011, **11**, 3190–3196.
69 B. Wang, X. Li, B. Luo, J. Yang, X. Wang, Q. Song, S. Chen and L. Zhi, *Small*, 2013, **9**, 2399–2404.
70 O. Beyssac, J.-N. Rouzaud, B. Goffe, F. Brunet and C. Chopin, *Contrib. Mineral. Petrol.*, 2002, **143**, 19–31.
71 D. Graf, F. Molitor, K. Ensslin, C. Stampfer, A. Jungen, C. Hierold and L. Wirtz, *Nano Lett.*, 2007, **7**, 238–242.
72 N. Bozovic, I. Bozovic and J. Misewich, *Nano Lett.*, 2008, **8**, 4477–4482.
73 M. Hu, J. Reboul, S. Furukawa, N. L. Torad, Q. Ji, P. Srinivasu, K. Ariga, S. Kitagawa and Y. Yamauchi, *J. Am. Chem. Soc.*, 2012, **134**, 2864–2867.

 

74 K. Saenger, J. Tsang, A. Bol, J. Chu, A. Grill and C. Lavoie, *Appl. Phys. Lett.*, 2010, **96**(15), 153105.
75 M. Muhyuddin, N. Zocche, R. Lorenzi, C. Ferrara, F. Poli, F. Soavi and C. Santoro, *Mater. Renew. Sustain. Energy*, 2022, **11**, 131–141.
76 A. S. Rajan, S. Sampath and A. K. Shukla, *Energy Environ. Sci.*, 2014, **7**, 1110–1116.
77 S. Sun, G. Zhang, N. Gauquelin, N. Chen, J. Zhou, S. Yang, W. Chen, X. Meng, D. Geng and M. N. Banis, *Sci. Rep.*, 2013, **3**, 1775.
78 Z. Yang, Z. Yu, H. Wei, X. Xiao, Z. Ni, B. Chen, Y. Deng, S. N. Habisreutinger, X. Chen and K. Wang, *Nat. Commun.*, 2019, **10**, 4498.
79 Y. Liu, M. Su, D. Li, S. Li, X. Li, J. Zhao and F. Liu, *RSC Adv.*, 2020, **10**, 6763–6771.
80 L. Xiao, Q. Yang, M. J. Wang, Z. X. Mao, J. Li and Z. Wei, *J. Mater. Sci.*, 2018, **53**, 15246–15256.
81 T. Najam, S. S. A. Shah, W. Ding, Z. Ling, L. Li and Z. Wei, *Electrochim. Acta*, 2019, **327**, 134939.
82 G. Liu, B. Wang, L. Wang, W. Wei, Y. Quan, C. Wang, W. Zhu, H. Li and J. Xia, *Green Energy Environ.*, 2022, **7**, 423–431.
83 R. Gokhale, Y. Chen, A. Serov, K. Artyushkova and P. Atanassov, *Electrochem. Commun.*, 2016, **72**, 140–143.
84 R. Mercado, C. Wahl, J. E. Lu, T. Zhang, B. Lu, P. Zhang, J. Q. Lu, A. Allen, J. Z. Zhang and S. Chen, *Chem. – Eur. J.*, 2020, **12**, 3230–3239.
85 Q. Chang, Y. Liu, J.-H. Lee, D. Ologunagba, S. Hwang, Z. Xie, S. Kattel, J. H. Lee and J. G. Chen, *J. Am. Chem. Soc.*, 2022, **144**, 16131–16138.
86 J. Guo, X. Yan, Q. Liu, Q. Li, X. Xu, L. Kang, Z. Cao, G. Chai, J. Chen and Y. Wang, *Nano Energy*, 2018, **46**, 347–355.
87 S. A. Mirshokraee, M. Muhyuddin, J. Orsilli, E. Berretti, L. Capozzoli, A. Lavacchi, C. L. Vecchio, V. Baglio, A. Galli and A. Zaffora, *Ind. Chem. Mater.*, 2023, **1**, 343–359.
88 M. Wilke, F. Farges, P.-E. Petit, G. E. Brown Jr. and F. Martin, *Am. Mineral.*, 2001, **86**, 714–730.
89 L. Feng, X. Sun, S. Yao, C. Liu, W. Xing and J. Zhang, in *Rotating electrode methods and oxygen reduction electrocatalysts*, Elsevier, 2014, pp. 67–132.
90 M. Borghei, J. Lehtonen, L. Liu and O. J. Rojas, *Adv. Mater.*, 2018, **30**, 1703691.
91 L. Khotseng, *Electrocatalysts for fuel cells and hydrogen evolution-Theory to design*, 2018, p. 27.
92 S. A. Mirshokraee, M. Muhyuddin, R. Morina, L. Poggini, E. Berretti, M. Bellini, A. Lavacchi, C. Ferrara and C. Santoro, *J. Power Sources*, 2023, **557**, 232571.
93 L. Cui, G. Lv and X. He, *J. Power Sources*, 2015, **282**, 9–18.
94 A. Kumar, G. Yasin, M. Tabish, D. K. Das, S. Ajmal, A. K. Nadda, G. Zhang, T. Maiyalagan, A. Saad and R. K. Gupta, *Chem. Eng. J.*, 2022, **445**, 136784.
95 Y. Mo, G. Liu, S. Liu and W. Lu, *ACS Appl. Nano Mater.*, 2023, **13**, 11252–11259.
96 J. Xue, S. Deng, R. Wang and Y. Li, *Carbon*, 2023, **205**, 422–434.
97 C. L. Vecchio, A. S. Aricò, G. Monforte and V. Baglio, *Renewable Energy*, 2018, **120**, 342–349.
98 C. Lo Vecchio, A. S. Aricò and V. Baglio, *Materials*, 2018, **11**, 1193.
99 S. A. Mirshokraee, M. Muhyuddin, R. Lorenzi, G. Tseberlidis, C. L. Vecchio, V. Baglio, E. Berretti, A. Lavacchi and C. Santoro, *SusMat*, 2023, **3**, 248–262.
100 A. Di Cicco, G. Aquilanti, M. Minicucci, E. Principi, N. Novello, A. Cognigni and L. Olivi, 14th International Conference on X-ray Absorption Fine Structure (XAFS14), Camerino, Italy, 2009, vol. 190, pp. 26–31.
101 B. Ravel and M. Newville, *J. Synchrotron Radiat.*, 2005, **12**, 537–541.
102 E. Giordano, E. Berretti, L. Capozzoli, A. Lavacchi, M. Muhyuddin, C. Santoro, I. Gatto, A. Zaffora and M. Santamaria, *J. Power Sources*, 2023, **563**, 232806.
103 M. Muhyuddin, J. Filippi, L. Zoia, S. Bonizzoni, R. Lorenzi, E. Berretti, L. Capozzoli, M. Bellini, C. Ferrara and A. Lavacchi, *ChemSusChem*, 2022, **15**, e202102351.
104 G. Wu, K. L. More, C. M. Johnston and P. Zelenay, *Science*, 2011, **332**, 443–447.